

# Analytic Continuation in Two-color Finite Density QCD and Chiral Random Matrix Model

Yasuhiko SHINNO<sup>\*)</sup> and Hiroshi YONEYAMA<sup>†\*\*)</sup>

*Nara National Colledge of Technology, Yamatokoriyama 639-1080, Japan*  
*Department of Physics, Saga University, Saga 840-8502, Japan<sup>‡</sup>*

## Abstract

Two-color finite density QCD is free from the sign problem, and it is thus regarded as a good model to check the validity of the analytic continuation method. We study the method in terms of the corresponding chiral random matrix model. It is found that at temperatures slightly higher than the pseudo critical temperature, the ratio type of extrapolated function works well in accordance with the results of the Monte Carlo simulations.

---

<sup>\*)</sup> E-mail: shinno@libe.nara-k.ac.jp

<sup>\*\*)</sup> E-mail: yoneyama@cc.saga-u.ac.jp

## §1. Introduction

Determining the phase structure of QCD in the chemical potential ( $\mu$ )- temperature ( $T$ ) plane is an important issue to understand properties of dynamics of QCD. Lattice gauge theory is one of promising tools to study non perturbative properties of QCD. At finite values of  $\mu$ , however, it suffers from notorious sign problem. Fermion determinant takes complex values and this invalidates importance sampling in Monte Carlo (MC) simulations. In order to circumvent the problem, various methods such as Taylor series method,<sup>1)2)</sup> reweighting method<sup>3)</sup> etc. are attempted. Among such methods is analytic continuation<sup>4),5),6),7),8),9)</sup> that we pay attention to in the present paper. In this method, one calculates some quantities in imaginary chemical potential region, fit the data by an appropriate function and extrapolate it to the real  $\mu$  region. Such an extrapolation, in general, requires careful assessment of extrapolated function. In order to explicitly check the validity of extrapolated functions, Cea et.al.<sup>10)11)</sup> studied two-color QCD,<sup>12),13),14),15),16),17),23),18),19),20),21),22),24),25),26),27)</sup> which is free from the sign problem. They calculated several quantities such as chiral condensate and Polyakov loop in the imaginary  $\mu$  region, and compared these extrapolations with the results of direct computations in the real  $\mu$  region. Based on what they studied, they made useful suggestions for applying the analytic continuation method to three-color QCD. In the current stage, however, it is a hard task to check their statements by using MC simulations because of the sign problem. It would then be useful to study these properties by adopting some other methods. In the present paper we use chiral random matrix theory (RMT) model.<sup>28)</sup>

Chiral RMT is equivalent to QCD in the  $\epsilon$  regime. This microscopic equivalence is made use of for calculating low energy constants such as pion decay constant. From a mean field point of view, on the other hand, it is used to study phase diagram in the  $\mu - T$  plane and has predicted relevant properties.<sup>29)</sup> Here, taking the latter stand point we study analytic continuations of two-color QCD in terms of the corresponding chiral RMT by investigating transitive regions from imaginary to real  $\mu$  region at finite  $T$ . Based on this study, we shall investigate three-color QCD, the results of which will be reported in a forthcoming paper.<sup>30)</sup> In the present paper, we adopt a model proposed by Klein, Toublan and Verbaarschot.<sup>31),32)</sup> Since we are concerned about analytic continuation properties, we study the phase structure in the imaginary  $\mu$  region, mainly in the vicinity of  $\mu = 0$ . Although the phase structure in the real  $\mu$  region is investigated in Ref. 32), we present a part of these results associated with analytic continuation.

It is found in MC studies<sup>10)11)</sup> that suitable fitting function depends on the region of temperatures, possibly reflecting the difference of involved physics. In particular, at

moderately high temperature region, the ratio type fitting function works well, and it is suggested to use it in the study of three-color QCD. In the present paper, we study the phase structure of the chiral RMT model in the real and imaginary  $\mu$  regions in the vicinity of  $\mu = 0$ . Based on the results, we divide the temperature into three regions,  $T < T_D$  (region I),  $T_D < T < T_{co}$  (region II) and  $T_{co} < T$  (region III), where  $T_D$  is the maximal temperature of the diquark condensate phase in the real  $\mu$  region, and  $T_{co}$  is temperature of cross over at  $\mu = 0$ . We study the analytic continuation of the chiral condensate and the cross over line. As fitting functions, we use the polynomial types as well as the ratio type. In region III, we found that the polynomial fits show slow convergence, while the ratio type fits work well, in accordance with the results of MC simulation studies.<sup>10)</sup> This is the main results of the present paper.

The adopted RMT model incorporates a temperature effect only through the lowest Matsubara frequencies. This approximation is expected to be poor in the low temperature region. In order to check if the results stated above concerning the analytic continuation is sensitive to this approximation, we also consider an extended RMT model,<sup>33)</sup> which incorporates all the Matsubara frequencies. We study the phase structure of this model in the real and imaginary  $\mu$  regions. In the real  $\mu$  region, we make it clear the relationship of temperature with that in the original RMT model. In the region III, we found that the ratio type of function fits well the behaviors of the chiral condensate in this model, too.

In the following section, we present the formulation of two-color QCD and its corresponding chiral RMT model. We briefly review its phase structure in the real  $\mu$  region and study the phase structure in the imaginary  $\mu$  region. We also present the results of the phase structure in the presence of a diquark source rather than quark mass. In section 3, we study analytic continuation of the chiral condensates and the pseudo critical line. In section 4, we discuss an effect of the higher Matsubara frequencies. Summary is presented in section 5.

## §2. Phase structure

### 2.1. Two-color QCD and RMT

In this subsection, let us briefly remind us of the chiral Lagrangian study and chiral random matrix model in two-color QCD for a completeness. Two-color QCD is characterized by pseudo reality

$$\tau_2 \tau_a \tau_2 = -\tau_a^*, \quad (2.1)$$

where  $\tau_a$  are Pauli matrices. As a consequence, the Lagrangian with massless  $N_f$  flavor quarks possesses enlarged  $SU(2N_f)$  flavor symmetry rather than  $SU(N_f) \times SU(N_f)$  symmetry. An introduction of the chemical potential induces symmetry breaking  $SU(2N_f) \rightarrow SU(N_f) \times$

$SU(N_f) \times U(1)_B$ . For non zero quark mass  $m \neq 0$ ,  $SU(2N_f)$  turns to  $Sp(2N_f)$ , and further  $Sp(2N_f) \rightarrow SU(N_f)_V \times U(1)_B$  due to a  $\mu$  term. Some time ago, Kogut et. al.<sup>15),16)</sup> studied the model based on the chiral Lagrangian. The static terms to lowest order in the momentum expansion of the effective Lagrangian are given by

$$\mathcal{L}_{\text{chiral}}^{\text{static}} = -F^2 m_\pi^2 \text{ReTr} \left( \Sigma \hat{M} \right) - F^2 \mu^2 \text{Tr} \left( \Sigma B^T \Sigma^\dagger B + BB \right), \quad (2.2)$$

where  $\Sigma$  is a  $2N_f \times 2N_f$  unitary antisymmetric matrix. The mass matrix  $\hat{M}$  and baryon charge matrix  $B$  are given by

$$\hat{M} = \begin{pmatrix} 0 & 1 \\ -1 & 0 \end{pmatrix}, \quad B = \begin{pmatrix} 1 & 0 \\ 0 & -1 \end{pmatrix}, \quad (2.3)$$

where 1 is  $N_f \times N_f$  unit matrix. The constant  $F$  is a low energy constant, and pion mass is given in terms of chiral condensate  $\langle \bar{\psi}\psi \rangle_0$  at  $\mu = 0$  by  $m_\pi^2 = m \langle \bar{\psi}\psi \rangle_0 / (2N_f F^2)$ . The Lagrangian can be minimized by using the following form

$$\Sigma = \Sigma_\sigma \cos \alpha + \Sigma_\Delta \sin \alpha, \quad (2.4)$$

where

$$\Sigma_\sigma = \begin{pmatrix} 0 & -1 \\ 1 & 0 \end{pmatrix}, \quad \Sigma_\Delta = \begin{pmatrix} iI & 0 \\ 0 & iI \end{pmatrix}, \quad I = \begin{pmatrix} 0 & -1 \\ 1 & 0 \end{pmatrix}. \quad (2.5)$$

For  $\mu \leq m_\pi/2$ , the chiral condensate dominates, while for  $\mu > m_\pi/2$  a rotation of condensates to the diquark condensate occurs as

$$\Sigma = \begin{cases} \Sigma_\sigma & (\mu \leq m_\pi/2) \\ \Sigma_\sigma \cos \alpha_0 + \Sigma_\Delta \sin \alpha_0 & (\mu > m_\pi/2), \end{cases} \quad (2.6)$$

where  $\cos \alpha_0 = m_\pi^2 / (4\mu^2)$ .

The QCD partition function with two flavors

$$Z_{\text{QCD}} = \left\langle \prod_{f=1}^2 \det(D + m_f + \mu_f \gamma_0) \right\rangle \quad (2.7)$$

is replaced by random matrix partition function

$$Z_{\text{RMT}} = \int \mathcal{D}W \exp\left[-\frac{n}{2} G^2 \text{Tr} W^T W\right] \det \hat{D}, \quad (2.8)$$

where due to the pseudo reality,  $W$  is represented by a real  $n \times n$  matrix, and the probability distribution of the matrix elements is Gaussian. The matrix  $\hat{D}$  is given by<sup>32)</sup>

$$\hat{D} = \begin{pmatrix} m_1 & 0 & W + \omega(T) + \mu_1 & 0 \\ 0 & m_2 & 0 & W + \omega(T) + \mu_2 \\ -W^T - \omega(T)^T + \mu_1 & 0 & m_1 & 0 \\ 0 & -W^T - \omega(T)^T + \mu_2 & 0 & m_2 \end{pmatrix}.$$

As a temperature effect, only the Matsubara lowest frequencies are incorporated in the form

$$\omega(T) = \begin{pmatrix} 0 & T \\ -T & 0 \end{pmatrix}. \quad (2.9)$$

In the present paper, we consider symmetric case  $\mu_1 = \mu_2$ , and  $m_1 = m_2$ .

Standard manipulations lead to a partition function represented by complex  $2N_f \times 2N_f$  ( $N_f = 2$ ) matrix  $A^{32}$

$$Z_{\text{RMT}} = \int \mathcal{D}A \exp[-\mathcal{L}], \quad (2.10)$$

$$\mathcal{L} = \frac{n}{2} G^2 \text{Tr} A A^\dagger - \frac{n}{4} \log \det Q_+ Q_-, \quad (2.11)$$

where

$$Q_\pm = \begin{pmatrix} A^\dagger + M & \mu B \pm iT \\ -\mu B \pm iT & A + M^\dagger \end{pmatrix}, \quad M = \begin{pmatrix} 0 & m & 0 & 0 \\ -m & 0 & 0 & 0 \\ 0 & 0 & 0 & m \\ 0 & 0 & -m & 0 \end{pmatrix} \quad (2.12)$$

and  $B = \text{diag}(1, -1, 1, -1)$ .

An ansatz for  $A$

$$A = \begin{pmatrix} 0 & -\sigma & -i\Delta & 0 \\ \sigma & 0 & 0 & -i\Delta \\ i\Delta & 0 & 0 & -\sigma \\ 0 & i\Delta & \sigma & 0 \end{pmatrix} \quad (2.13)$$

leads to an effective potential:

$$\begin{aligned} \frac{1}{n} \mathcal{L} &= 2G^2(\sigma^2 + \Delta^2) - \ln D, \\ D &= [(\sigma + m + \mu)^2 + \Delta^2 + T^2] [(\sigma + m - \mu)^2 + \Delta^2 + T^2]. \end{aligned} \quad (2.14)$$

## 2.2. saddle point equation

In order to obtain the most dominant contribution in Eq.(2.10) in the  $n \rightarrow \infty$  limit, we solve the saddle point equations given by

$$\frac{\partial \mathcal{L}}{\partial \sigma} = 0, \quad \frac{\partial \mathcal{L}}{\partial \Delta} = 0. \quad (2.15)$$

This yields

$$\sigma G^2 D - ((\sigma + m)^2 - \mu^2 + \Delta^2 + T^2) (\sigma + m) = 0, \quad (2.16)$$

$$\Delta [G^2 D - ((\sigma + m)^2 + \mu^2 + \Delta^2 + T^2)] = 0, \quad (2.17)$$

where  $D$  reads

$$D = [(\sigma + m)^2 + \Delta^2 + \mu^2]^2 - 4\mu^2(\sigma + m)^2 + 2 [(\sigma + m)^2 + \Delta^2 + \mu^2] T^2 + T^4. \quad (2.18)$$

Saddle point equations in the imaginary  $\mu$  region are given by replacing  $\mu$  by  $i\phi$  in Eq's. (2.16), (2.17) and (2.18). In the following subsections, the phase structure in the imaginary  $\mu$  region is studied. In order to understand the following analysis of the analytic continuation, we also discuss the phase in the real  $\mu$  region. Although the latter is studied in detail in Ref. 32), we present a part of it in a self-contained manner. It should be noted that the RMT model does not show a periodicity in the imaginary  $\mu$ , caused by the center symmetry of the gauge group (Roberge-Weiss symmetry<sup>34</sup>). This point is discussed in summary in connection with the analytic continuation.

### 2.2.1. $m = 0$

In the following section, we shall discuss the analytic continuation in the case of non zero quark mass. In order to have a better understanding of the phase structure in the massive case, we also discuss the phase structure in the massless case. For  $m = 0$ , the saddle point equations are analytically solved. For  $T = 0$ , the saddle point equations become

$$\begin{cases} \sigma = 0, & G^2 D = \sigma^2 - \mu^2 + \Delta^2, \\ \Delta = 0, & G^2 D = \sigma^2 + \mu^2 + \Delta^2, \end{cases} \quad (2.19)$$

$$D = (\sigma^2 - \mu^2 + \Delta^2)^2 + 4\Delta^2\mu^2. \quad (2.20)$$

This is classified into the following four cases:(a)  $\sigma = 0, \Delta = 0$ , (b)  $\sigma = 0, \Delta \neq 0$ , (c)  $\sigma \neq 0, \Delta = 0$ , (d)  $\sigma \neq 0, \Delta \neq 0$ . Correspondingly, the effective potential reads

$$\begin{aligned} \Omega &\equiv \frac{1}{n} \mathcal{L}^{(a)} = -2 \ln \mu^2, \\ \Omega^{(\Delta)} &\equiv \frac{1}{n} \mathcal{L}^{(b)} = 2(1 + \ln G^2 - G^2 \mu^2) \quad (\Delta^2 + \mu^2 = 1/G^2), \\ \Omega^{(\sigma)} &\equiv \frac{1}{n} \mathcal{L}^{(c)} = 2(1 + \ln G^2 + G^2 \mu^2) \quad (\sigma^2 - \mu^2 = 1/G^2), \\ \Omega^{(\Delta\sigma)} &\equiv \frac{1}{n} \mathcal{L}^{(d)} = 2(1 + \ln G^2) \quad \text{at } \mu = 0 \text{ only.} \end{aligned} \quad (2.21)$$

For  $0 \leq \mu < \mu_c$ ,  $\Omega^{(\Delta)}$  gives the lowest values among these  $\Omega$ , i.e., diquak condensation occurs, where  $\mu_c$  is determined so that  $2(1 - G^2 \mu^2) + \ln(G^2 \mu^2)^2 = 0$  ( $\Omega^{(\Delta)} = \Omega$ ) is satisfied. For  $\mu > \mu_c$ , symmetric phase realizes. For imaginary  $\mu = i\phi$ , one can easily see in Eq. (2.21)

that minimum is found just by an interchange of  $\sigma$  and  $\Delta$ , i.e., the roles of  $\sigma$  and  $\Delta$  are interchanged in the real and imaginary  $\mu$  regions. For  $0 \leq \phi < \phi_c$ , chiral condensation occurs, and for  $\phi_c < \phi$ ,  $\sigma = 0, \Delta = 0$ . The value of  $\phi_c$  satisfies  $2(1 - G^2\phi_c^2) + \ln(G^2\phi_c^2)^2 = 0$  ( $\tilde{\Omega}^{(\sigma)} = \tilde{\Omega}$ ), where  $\tilde{\Omega}^{(\sigma)} \equiv \Omega^{(\sigma)}(\mu \rightarrow i\phi)$  etc.. At  $\mu = 0$ , the system undergoes a first order phase transition. When one crosses the origin from real  $\mu$  to imaginary  $\mu$  region, the magnitudes of  $\Delta$  in the real  $\mu$  region jumps down to 0 at  $\mu = 0$ , while that of  $\sigma$  jumps up to a finite value from vanishing one.

At finite temperatures, this first order critical point persists up to a finite value  $T_c$  along the  $T$ -axis as shown in the left panel in Fig.1. Temperature effect also shifts the location of  $\mu_c$  such that

$$1 + \ln G^2(\mu_c^2 + T^2) - G^2(\mu_c^2 + T^2) = 0, \quad (2.22)$$

while  $\phi_c$  is determined by

$$2G^2(\phi_c^2 + T^2) - \left(1 + \sqrt{1 + 16\phi_c^2 T^2 G^4}\right) = 0. \quad (2.23)$$

The second order critical line in the real  $\mu$  region starts at  $\mu = \mu_c$ , passes the endpoint

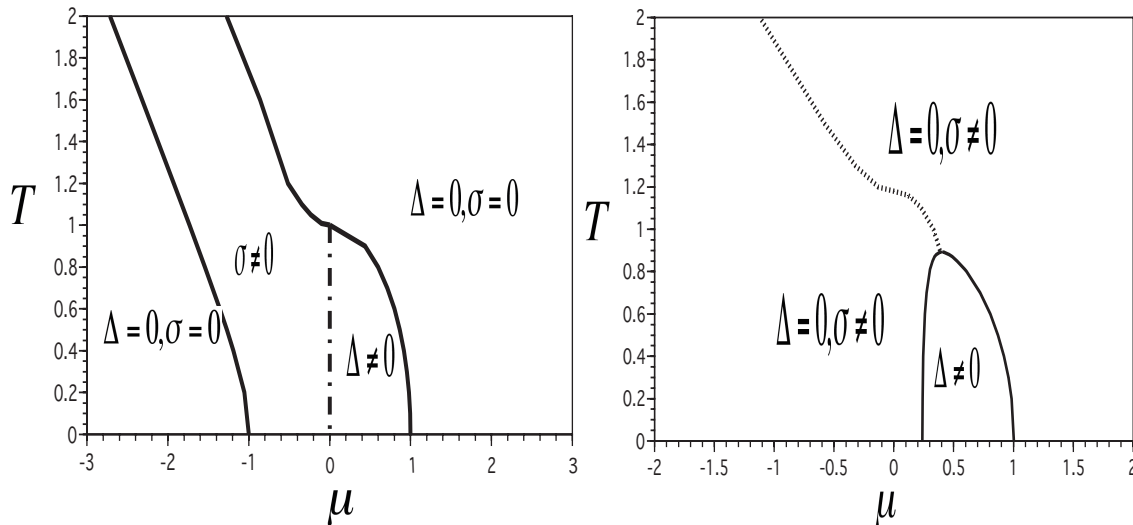


Fig. 1. Phase diagram for  $m = 0$  (left) and  $m = 0.1$  (right). Solid lines indicate second order critical lines. Dashed dotted and dotted lines indicate first order critical line and cross over, respectively.  $G = 1.0$ . Note that negative side of the horizontal axis indicates the imaginary chemical potential,  $i|\mu|$ .

( $\mu = 0, T_c$ ) of the first order critical line at  $\mu = 0$  and extends to the imaginary  $\mu$  region as  $T$  increases. On the other hand, the critical line, separating symmetric and chiral condensate phases in the imaginary  $\mu$  region, starts at  $\phi_c G = 1.0$  and  $T = 0$ , and moves toward larger values of  $\phi$  as  $T$  increases. These are shown in the left panel in Fig.1.

### 2.2.2. $m \neq 0$

For  $m \neq 0$ , the effect of chiral condensate becomes stronger and the phase structure changes. The first order critical line, separating chiral and diquark condensate phases at  $\mu = 0$  in the  $m = 0$  case, changes to the second order one and shifts towards real  $\mu$  region as shown on the right panel of Fig.1. This is given as the lowest energy solution of Eq's. (2.16) and (2.17) for small values of  $\mu$ . At  $T = 0$ , the phase transition occurs at  $\mu_c G = 0.26 \equiv \mu_{c1} G$ . For  $\mu \geq \mu_{c1}$ , chiral condensate rotates into diquark condensate, which is in agreement with the chiral Lagrangian study as in Eq. (2.6). Figure 2 indicates contour plots of the effective potential in the  $\sigma - \Delta$  plane for  $m = 0.1$  and  $T = 0$  ( $\mu G = 0.0, 0.4$  and  $0.8$  from left to right). The darker the plot becomes, the smaller the magnitude of the effective potential becomes. We see that the minimum rotates from  $(\sigma \neq 0, \Delta = 0)$  to  $(\sigma = 0, \Delta \neq 0)$  as  $\mu$  increases. Unlike the chiral Lagrangian, however, diquark condensate becomes vanishing at  $\mu G = \mu_c G (= 1.0)$  at  $T = 0$ , and the diquark condensate phase turns to quasi symmetric one ( $\sigma \approx O(m), \Delta = 0$ ). This is due to the saturation effect coming from the limited dirac spectrum of the RMT. As temperature increases, diquark condensate phase becomes narrower and terminates at  $(\mu_D, T_D)$ . For  $T \geq T_D$ , thermal fluctuations become large enough to make diquark condensate cease. A cross over line leaves the point  $(\mu_D, T_D)$  and moves towards  $\mu = 0$  as temperature increases, where the signal of cross over is detected by a peak of chiral susceptibility. This line is a reminiscent of the second order critical line in the  $m = 0$  case. In the imaginary  $\mu$  region, it further proceeds toward larger values of  $\phi$  as temperature increases. For larger values of  $\phi$ , the signal of the critical line in the  $m = 0$  case, emanating

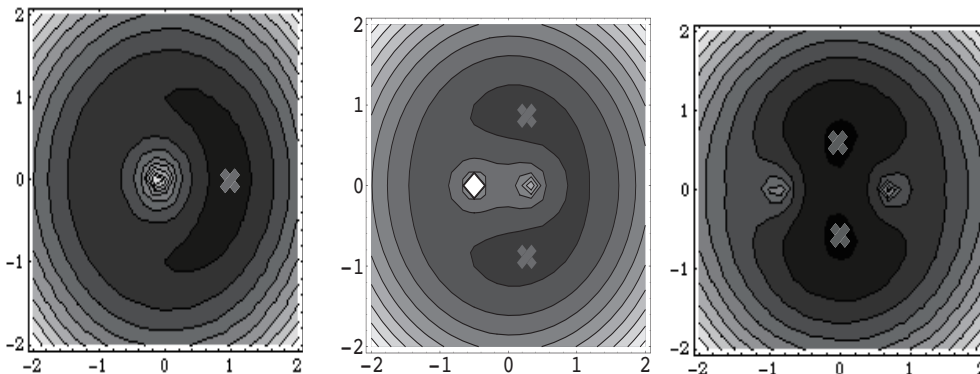


Fig. 2. Contour plots of the effective potential in  $\sigma - \Delta$  plane for  $m = 0.1$  at  $T = 0$ . From left to right,  $\mu = 0.0, 0.4$  and  $0.8$ . The cross symbol indicates the location of the minima.  $G = 1.0$ . The horizontal (vertical) axis stands for  $\sigma$  ( $\Delta$ ).

at  $\phi_c$ , becomes so weak in the  $m \neq 0$  case that the peak of the susceptibility is very broad and low. In the figure, we do not show it.



### 2.3. diquark source $j_d \neq 0$

So far we have discussed the phase structure in the case of non zero quark mass. In two-color QCD, meson and diquark states belong to the same representation, and then mass and diquark source are on an equal footing. It is interesting, therefore, to discuss the phase structure when a diquark source is switched on. When  $m = 0$ , a diquark source  $j_d$  is introduced in Eq. (2.12) as

$$M = \begin{pmatrix} 0 & 0 & -ij_d & 0 \\ 0 & 0 & 0 & -ij_d \\ ij_d & 0 & 0 & 0 \\ 0 & ij_d & 0 & 0 \end{pmatrix}. \quad (2.24)$$

The effective potential becomes

$$\frac{1}{n}\mathcal{L} = 2G^2(\sigma^2 + \Delta^2) - \ln D^{(d)}, \quad (2.25)$$

$$D^{(d)} = [(\Delta + j_d)^2 + \sigma^2 - \mu^2]^2 + 4\mu^2(\Delta + j_d)^2 + 2[(\Delta + j_d)^2 + \sigma^2 + \mu^2]T^2 + T^4. \quad (2.26)$$

At  $T = 0$ , the argument of the logarithmic term in Eq. (2.25) reads

$$D^{(d)} = [(\Delta + j_d)^2 + \sigma^2 - \mu^2]^2 + 4\mu^2(\Delta + j_d)^2. \quad (2.27)$$

Comparing this with  $D$  in Eq. (2.18) at  $T = 0$ , we recognize that there is a symmetry with respect to a simultaneous interchange of  $j_d \leftrightarrow m$ ,  $\Delta \leftrightarrow \sigma$  and  $\mu^2 \leftrightarrow -\mu^2$ . This implies that the behavior of  $\sigma$  ( $\Delta$ ) in the  $j_d \neq 0, m = 0$  case is a mirror image of the behavior of  $\Delta$  ( $\sigma$ ) in the  $j_d = 0, m \neq 0$  case if one plots them as functions of  $\mu^2$  as shown in Fig. 3. The rotation of condensate thus occurs in the imaginary  $\mu$  region, from  $\Delta \neq 0$  to  $\sigma \neq 0$  as  $\phi$  increases from 0.

At finite  $T$ , a term proportional to  $T^2$  breaks this symmetry as seen in Eq.'s (2.18) and (2.26). At low temperatures, such a breaking effect is small, but at higher temperatures, it becomes clearer. By investigating the behaviors of  $\sigma$  and  $\Delta$  in the similar way to the  $m \neq 0$  case, we obtain the critical lines as shown in Fig. 4. Unlike the  $m \neq 0, j_d = 0$  case, the phase with both of  $\sigma$  and  $\Delta$  condensation, located now in the imaginary  $\mu$  region, does not close itself but stretches to larger temperature region.

### §3. Analytic continuation

In this section, we discuss analytic continuation for  $m \neq 0$ . Hereafter,  $G$  is taken to be 1.0. Figure 5 indicates free energy and chiral condensate in the real and imaginary  $\mu$  regions

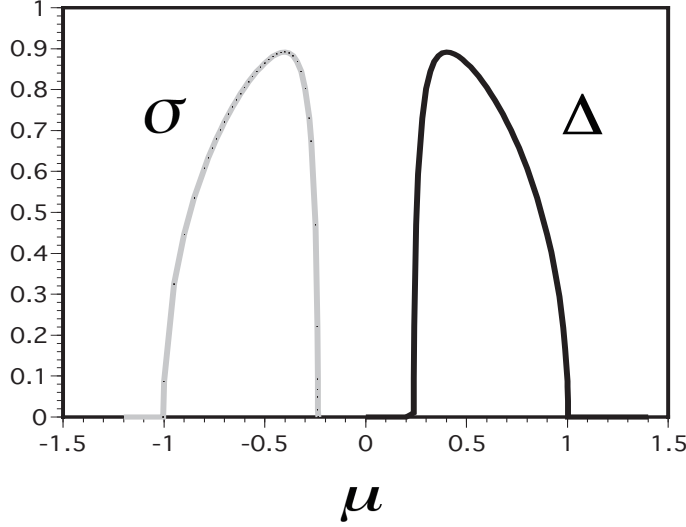


Fig. 3.  $\sigma$  for  $(j, m) = (0.1, 0)$  and  $\Delta$  for  $(j, m) = (0, 0.1)$  at  $T = 0$ .  $G = 1.0$ . Negative side of the horizontal axis indicates the imaginary chemical potential,  $i|\mu|$ .

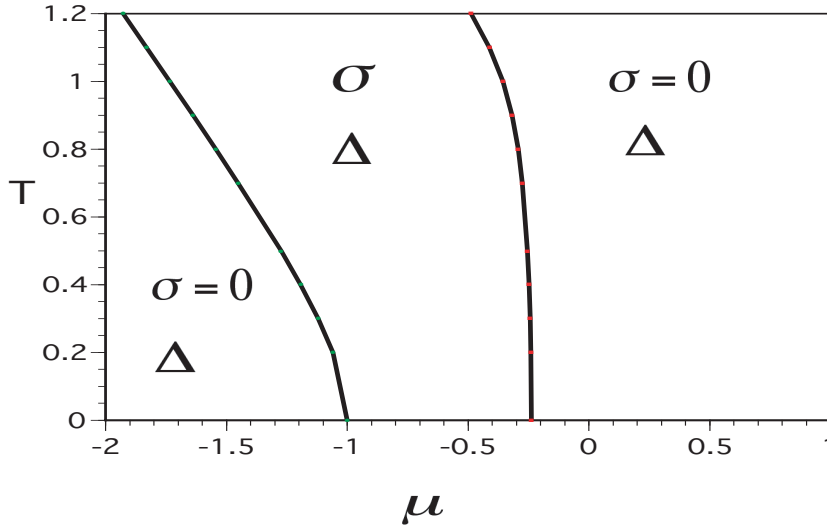


Fig. 4. Critical lines for  $j = 0.1$  and  $m = 0$ .  $G = 1.0$ . Solid line indicates the second order critical line. Negative side of the horizontal axis indicates the imaginary chemical potential,  $i|\mu|$ .

for various temperatures for  $m = 0.1$ . Both of the quantities behave smoothly at  $\mu = 0$  for all temperatures considered here. Based on these results, we check analytic continuation in terms of the RMT and compare the results with those of MC simulations.<sup>10)11)</sup>

### 3.1. chiral condensate

We use calculated values of  $\sigma$  in the imaginary  $\mu$  region as “data”. We take  $s$  points of data in a certain range  $0 < \phi \leq \phi_f$ , fit them by an appropriate function and extrapolate it to the real  $\mu$  region. Following Cea et. al., the following two types of fitting function are

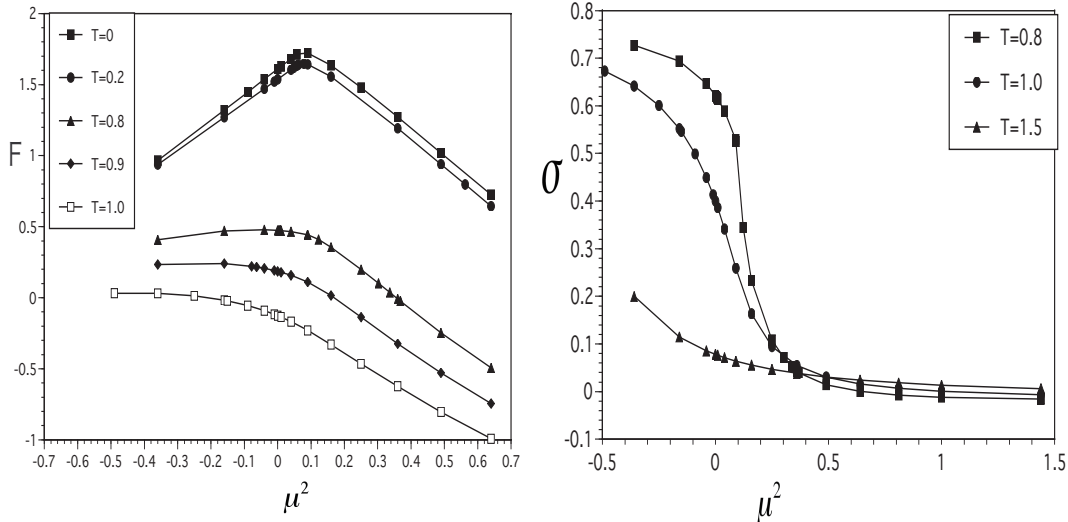


Fig. 5. Free energy (left) and chiral condensate (right) in the vicinity of  $\mu = 0$  for  $m = 0.1$  and various values of  $T$ .

used, one being polynomial type and the other ratio type.

$$\sigma = \begin{cases} A + B\phi^2 + C\phi^4 + \dots & \text{(polynomial),} \\ \frac{A+B\phi^2}{1+C\phi^2} & \text{(ratio).} \end{cases}$$

For a systematic study, we check to what extent the outcome depends on the following points:

1. the range of used “data” in the imaginary  $\mu$  region
2. the number of degrees of freedom of the data
3. the highest degree of the polynomial in the case of polynomial fit

We used  $\phi_f = 0.3, 0.5$  and  $0.8$ , and found that the outcome depends rather strongly on the adopted range  $\phi_f$ . Generally speaking, the  $\phi_f = 0.3$  case turns out the best among all the cases we investigated. On the other hand, when we varied the number of degrees of freedom, d.o.f., from 1 to about 75, depending on data, the results depend hardly on the number of data  $s$ . This is shown in Table I for the  $T = 0.8$  and  $1.5$  cases. Hereafter, we present the results of  $\phi_f = 0.3$ .

We divide temperature into three different regions,  $T < T_D$  (region I),  $T_D < T < T_{co}$  (region II) and  $T_{co} < T$  (region III), where  $T_D$  is the maximal temperature of the diquark condensate phase ( $T_D = 0.892$ ) and  $T_{co}$  is temperature of cross over at  $\mu = 0$  ( $T_{co} = 1.18$ ). It should be noted that this classification of the region of temperature are different from that in Ref. 10). Regime a and b in Ref. 10) correspond to our region III, and regime c in Ref. 10) are further classified into region I and II in our case. In the latter, we distinguish whether analytic continuation hits the diquark condensate phase (region I) or not (region II). In region

Table I. Dependence of fitting parameters on the number of data for  $T = 0.8$  and  $1.5$ . The adopted range for the data is  $0.0 < \phi < 0.3$ .  $\Delta\phi$  is defined by the number of points  $s$  as  $\phi_f/s$ .

$f(\phi) = A + B\phi^2 + C\phi^4$				
	$T = 0.8$		$T = 1.5$	
$\Delta\phi$	0.01	0.05	0.01	0.05
d.o.f.	28	4	28	4
$\chi^2/\text{d.o.f.}$	$5.63814 \times 10^{-9}$	$1.08933 \times 10^{-8}$	$5.2598 \times 10^{-11}$	$1.02758 \times 10^{-10}$
$A$	0.62178(2)	0.62178(7)	0.07803(0)	0.07803(0)
$B$	-0.68756(169)	-0.68116(454)	-0.17377(16)	-0.17360(44)
$C$	-1.67541(2050)	-1.6443(506)	0.32745(198)	0.33086(492)
$g(\phi) = A + B\phi^2 + C\phi^4 + D\phi^6$				
	$T = 0.8$		$T = 1.5$	
$\Delta\phi$	0.01	0.05	0.01	0.05
d.o.f.	27	3	27	3
$\chi^2/\text{d.o.f.}$	$3.18334 \times 10^{-11}$	$5.12716 \times 10^{-11}$	$3.03625 \times 10^{-14}$	$4.60497 \times 10^{-14}$
$A$	0.62171(0)	0.62170(0)	0.07802(0)	0.07802(0)
$B$	-0.70553(29)	-0.70565(74)	-0.17551(0)	-0.17550(2)
$C$	-2.26163(849)	-2.26256(2152)	0.27069(2)	0.27073(65)
$D$	-4.65104(6623)	-4.63419(15920)	-0.45033(205)	-0.45081(477)
$h(\phi) = \frac{A+B\phi^2}{1+C\phi^2}$				
	$T = 0.8$		$T = 1.5$	
$\Delta\phi$	0.01	0.05	0.01	0.05
d.o.f.	28	4	28	4
$\chi^2/\text{d.o.f.}$	$4.40095 \times 10^{-11}$	$9.37848 \times 10^{-11}$	$1.93257 \times 10^{-12}$	$3.59884 \times 10^{-12}$
$A$	0.62169(0)	0.62169(0)	0.07802(0)	0.07802(0)
$B$	-2.88150(288)	-2.88685(769)	-0.05713(15)	-0.05738(37)
$C$	-3.49352(434)	-3.50174(1153)	1.52002(163)	1.51722(399)

I, we do not consider very low temperature because this model incorporates only the lowest Matsubara frequencies and is thus expected to be poor in predictability. The left panel in Fig. 6 indicates the results of  $\sigma$  for  $T = 0.8$ . At this temperature, there exists a critical point at  $\mu_{c1}^2 = 0.089$ . Extrapolations to the real  $\mu$  region for both of the two types of fitting are good up to this critical point  $\mu_{c1}$ , but becomes extremely bad beyond  $\mu_{c1}$ , as it is expected. This behavior corresponds to the behavior in the low temperature region in Ref. 10). When

they use a polynomial function as an interpolation at this temperature region, the deviation between the fit and the real data occurs at the point where a chiral condensate susceptibility peak occurs in the real  $\mu$  region.<sup>10)</sup> In our case, this peak is observed as a sharp one at  $\mu_{c1}$ , where the diquark condensate starts to rise. In the polynomial case, if the higher power contributions are included, the above stated feature does not change (see Table II).

In region II, we choose  $T = 1.0$ . At this temperature, a cross over exists at  $\mu^2 = 0.109$ . In

Table II. Values of data and the results of various fits at real values of  $\mu$  for  $T = 0.8$ . The range of used data is  $0.0 < \phi < 0.3$ , and  $\Delta\phi = 0.01$ . Note that a critical point exists at  $\mu \simeq 0.299$ .

	$\mu = 0.0$	$\mu = 0.1$	$\mu = 0.2$	$\mu = 0.3$	$\mu = 0.4$	$\mu = 0.5$
data	0.63270	0.61437	0.58886	0.52881	0.23333	0.10833
4th degree	0.62178	0.61474	0.59160	0.54633	0.46888	0.34518
6th degree	0.62171	0.61442	0.58957	0.53650	0.43187	0.23130
8th degree	0.62170	0.61437	0.58905	0.53233	0.40771	0.12378
10th degree	0.62170	0.61437	0.58891	0.53046	0.39102	0.01637
ratio	0.62169	0.61434	0.58870	0.52854	0.36526	-0.77936

the polynomial method, the effect of the higher power terms becomes smaller, and the 4th degree of polynomial yields as good results as the higher degree of polynomials as shown in the right panel in Fig. 6. Deviations from the data become large at a value of  $\mu$  slightly higher than the cross over point where a chiral condensate susceptibility peak occurs. The ratio method is also in the same quality as the polynomial ones. In Table III, we show the numerical values of the results.

In the higher temperature region, region III, however, we obtained different results. Figure 7

Table III. Values of data and the results of various fits at real values of  $\mu$  for  $T = 1.0$ . The range of used data is  $0.0 < \phi < 0.3$ , and  $\Delta\phi = 0.01$ . Note that a cross over point exists at  $\mu \simeq 0.33$ .

	$\mu = 0.0$	$\mu = 0.1$	$\mu = 0.2$	$\mu = 0.3$	$\mu = 0.4$	$\mu = 0.5$
data	0.40000	0.38615	0.34111	0.25935	0.16310	0.09460
4th degree	0.40007	0.34220	0.38640	0.25780	0.11710	-0.10244
6th degree	0.40000	0.38611	0.34035	0.24884	0.08340	-0.20614
8th degree	0.40000	0.38614	0.34060	0.25083	0.09493	-0.15482
10th degree	0.40000	0.38615	0.34092	0.25511	0.13320	-0.09155
ratio	0.39996	0.38593	0.33880	0.23825	0.01903	-0.62254

indicates the fitting at  $T = 1.5$ . In the left panel, we compare the different types of fitting,

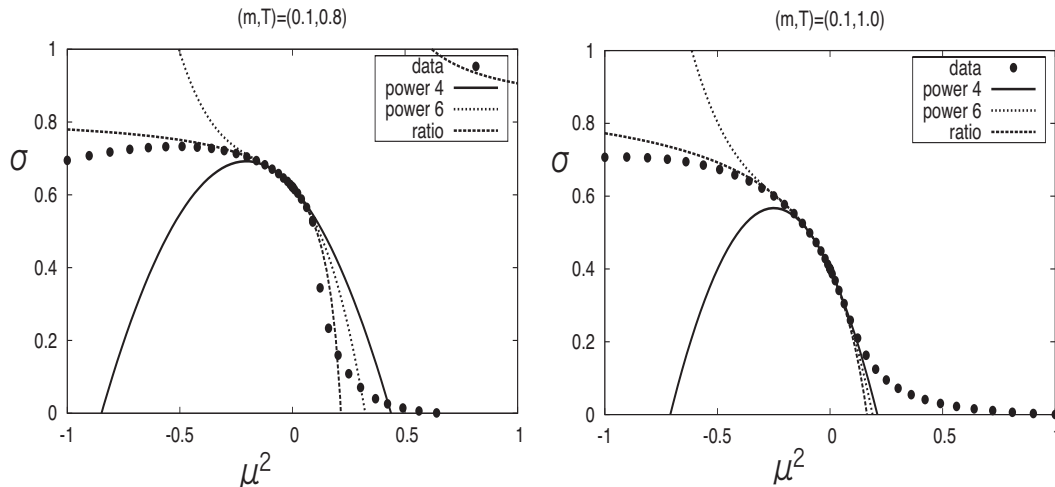


Fig. 6. Fitting at  $T = 0.8$  (left) and  $T = 1.0$  (right) for  $m = 0.1$ . Two types of polynomial fit (the 4th and 6th degree) and ratio type are compared with the “data”.

and find that the ratio type of fit works very well. This behavior is in good agreement with that in the higher temperature region (regime a and b) in the MC simulations.<sup>10)</sup> In contrast to this behavior, the polynomial fit shows the behavior with very slow convergence as shown in the right panel. There, we compare the results of the polynomial fit with the maximal power from 4 to 10. In Table IV, we show the numerical values of these fittings at several values of  $\mu$ . In order to check if the ratio method works well at other temperatures in region III, we chose  $T = 1.7, 1.8, 1.9, 2.0$  and  $2.2$  as temperatures higher than 1.5, and found that this is indeed the case. When we chose, on the other hand, the value of  $T$  slightly lower than 1.5 in region III, the same tendency is seen, but the contrast between the ratio and polynomial types becomes less clearer than the case of  $T=1.5$ . The results at  $T = 1.3$  are listed in Table V. The values of the fitting parameters used for  $T = 0.8, 1.0, 1.3$  and  $1.5$  are summarized in Table VI.

### 3.2. chiral susceptibility peak

The analytic continuation method has been applied to the determination of the critical line.<sup>4)</sup> We here focus on the chiral susceptibility peak for this purpose. The chiral susceptibility  $\chi_{ch}$  is calculated by the  $m$ -dependence of  $\sigma$ . The location of a peak of  $\chi_{ch}$  in  $\mu^2 - T$  plane for  $m = 0.1$  is shown in Fig. 8. We fit the imaginary “data” for  $0 \leq \phi \leq 0.32$  by polynomial formulae, one is  $A + B\mu^2$  and the other  $A + B\mu^2 + C\mu^4 + D\mu^6$ , and extrapolate them to the real  $\mu$  region. These are compared with the results for real  $\mu$  values of the model

Table IV. Values of data and the results of various fits at real values of  $\mu$  for  $T = 1.5$ . The range of used data is  $0.0 < \phi < 0.3$ , and  $\Delta\phi = 0.01$ .

	$\mu = 0.0$	$\mu = 0.2$	$\mu = 0.4$	$\mu = 0.6$	$\mu = 0.8$	$\mu = 1.0$
data	0.07802	0.07142	0.05570	0.03837	0.02399	0.01353
4th degree	0.07803	0.07160	0.05861	0.05791	0.10094	0.23171
6th degree	0.07802	0.07141	0.05503	0.02891	-0.04148	-0.2771
8th degree	0.07802	0.07142	0.05578	0.04097	0.05876	0.26905
10th degree	0.07802	0.07142	0.05573	0.04058	0.05345	0.22534
ratio	0.07802	0.07139	0.05540	0.03713	0.02101	0.00829

Table V. Values of data and the results of various fits at real values of  $\mu$  for  $T = 1.3$ . The range of used data is  $0.0 < \phi < 0.3$ , and  $\Delta\phi = 0.01$ .

	$\mu = 0.0$	$\mu = 0.2$	$\mu = 0.4$	$\mu = 0.6$	$\mu = 0.8$	$\mu = 1.0$
data	0.13425	0.11678	0.07971	0.04646	0.02424	0.01072
4th degree	0.13426	0.11721	0.08920	0.11963	0.32415	0.86470
6th degree	0.13425	0.11694	0.08420	0.07916	0.12544	0.15474
8th degree	0.13425	0.11671	0.07362	-0.09124	-1.29117	-7.56647
10th degree	0.13425	0.11678	0.08174	0.16905	2.37356	22.91351
ratio	0.13422	0.11625	0.07496	0.03110	-0.00495	-0.03183

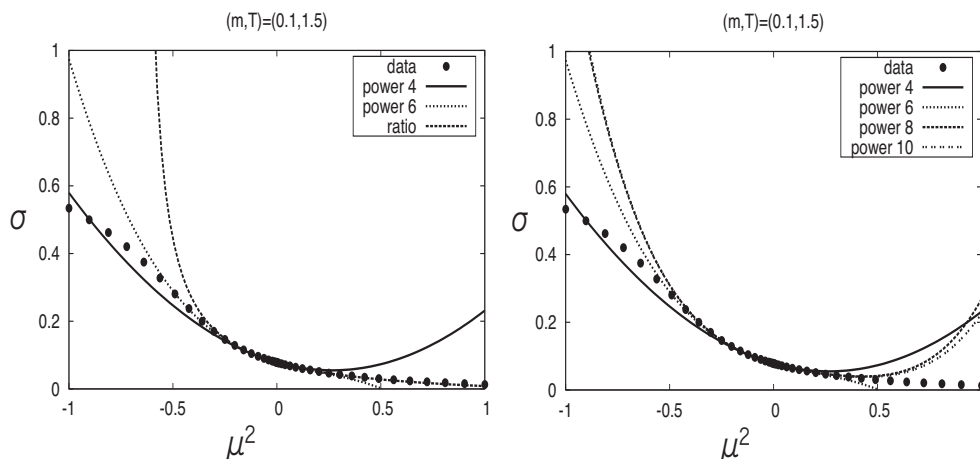


Fig. 7. Fitting at  $T = 1.5$  for  $m = 0.1$ . Two types of polynomial fit (the 4th and 6th degree) and ratio type are compared with the “data” in the left panel. The maximal power dependence in the polynomial fit is shown in the right panel.

Table VI. Parameters of various fits of the chiral condensate in accordance to  $\sigma(\phi) = A + B\phi^2 + C\phi^4 + D\phi^6 + E\phi^8 + F\phi^{10}$  (polynomial; p) or  $\sigma(\phi) = \frac{A+B\phi^2}{1+C\phi^2}$  (ratio; r). Note that blank columns stand for terms not included in the fit.

$T$	Fit	A	B	C	D	E	F	d.o.f.	$\chi^2/\text{d.o.f.}$
0.8	p	0.62178	-0.68756	-1.67541				28	$5.63814 \times 10^{-9}$
	p	0.62171	-0.70553	-2.26163	-4.65104			27	$3.18334 \times 10^{-11}$
	p	0.62170	-0.70780	-2.39816	-7.22101	-14.9146		26	$1.97889 \times 10^{-13}$
	p	0.62170	-0.70807	-2.42373	-8.05784	-25.9669	-50.6777	25	$1.57648 \times 10^{-15}$
	r	0.62169	-2.88150	-3.49352				28	$4.40095 \times 10^{-11}$
1.0	p	0.40007	-1.33932	-2.68272				28	$4.65810 \times 10^{-9}$
	p	0.40000	-1.35568	-3.21656	-4.23547			27	$8.22244 \times 10^{-12}$
	p	0.40000	-1.35459	-3.1514	-3.00882	7.11877		26	$1.05268 \times 10^{-12}$
	p	0.40000	-1.35399	-3.09274	-1.08930	32.4704	116.244	25	$2.02417 \times 10^{-14}$
	r	0.39996	-2.43151	-2.66407				28	$1.26412 \times 10^{-9}$
1.3	p	0.13426	-0.47440	1.20483				28	$1.08238 \times 10^{-10}$
	p	0.13425	-0.47683	1.12564	-0.62833			27	$6.11875 \times 10^{-12}$
	p	0.13425	-0.47782	1.06582	-1.75429	-6.53443		26	$4.66163 \times 10^{-14}$
	p	0.13425	-0.47769	1.07827	-1.35679	-1.15240	24.6779	25	$5.27750 \times 10^{-17}$
	r	0.134221	-0.22694	1.91334				28	$9.61851 \times 10^{-10}$
1.5	p	0.07809	-0.17377	0.32745				28	$5.2598 \times 10^{-11}$
	p	0.07802	-0.17551	0.27069	-0.45033			27	$3.03625 \times 10^{-14}$
	p	0.07802	-0.17544	0.27492	-0.37034	0.46189		26	$1.51937 \times 10^{-17}$
	p	0.07802	-0.17544	-0.27490	-0.37132	0.45424	-0.03506	25	$1.57037 \times 10^{-17}$
	r	0.07802	-0.05710	1.52002				28	$1.93257 \times 10^{-12}$

as shown in Fig. 8. The latter fits very well, while the former does not function at all. That higher order terms play a relevant role in the case of chiral susceptibility peak is in good agreement with that of Cea et.al. (see Fig's. 3 and 6 in the first reference in Ref. 11)).

#### §4. Effect of higher Matsubara frequencies

The model we have studied so far, let us tentatively call it the KTV model, incorporates temperature effects only from the lowest Matsubara frequencies. This limitation is expected to give an influence on the behaviors of the baryon density and chiral condensate at low temperatures, because the Matsubara frequencies form a continuum at zero temperature



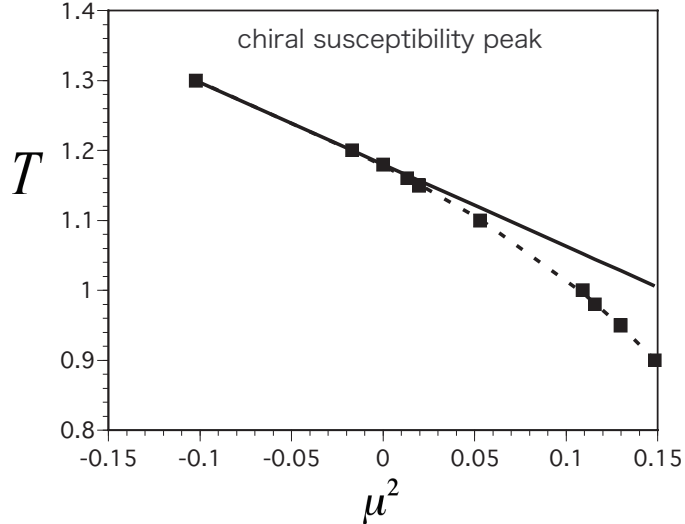


Fig. 8. Locations of the chiral susceptibility peaks in  $\mu^2 - T$  plane for  $m = 0.1$ , and two types of polynomial fit: linear in  $\mu^2$ ,  $1.180 - 1.171\mu^2$  (solid line) and the maximal power with  $\mu^6$ ,  $1.178 - 1.294\mu^2 - 2.157\mu^4 - 11.564\mu^6$  (broken line).

limit. Vanderheyden and Jackson<sup>33)</sup> introduced an extended RMT model (VJ model) incorporating contributions from higher Matsubara frequencies. We study this model in the imaginary  $\mu$  region and investigate the analytic continuation in order to check to what extent the results obtained in the previous section are robust, particularly, in region III.

@ The partition function of the VJ model is given by

$$Z = \int d\sigma d\Delta e^{-n\tilde{\Omega}}. \quad (4.1)$$

The effective potential is given by

$$\begin{aligned} \tilde{\Omega} &= 2\beta G^2(\sigma^2 + \Delta^2) - f(\sigma, \Delta), \\ f(\sigma, \Delta) &= \sum_{\pm} \sum_{n=-\infty}^{\infty} \ln [\beta^2 ((\sigma + m \pm \mu)^2 + \Delta^2 + (2n + 1)^2 \pi^2 T^2)], \end{aligned} \quad (4.2)$$

where the summation over  $n$  stands for the one over Matsubara frequencies, and the summation over  $\pm$  does their positive and negative parts, and  $\beta = 1/T$ . A term, referred to as the regular term in Ref. 33), is dropped in Eq. (4.2), since it is independent of  $\sigma$  and  $\Delta$ , and irrelevant in the following argument concerning the analytic continuation. By defining

$$\Omega = \tilde{\Omega}/\beta,$$

the partition function reads

$$Z = \int d\sigma d\Delta e^{-n\beta\Omega}, \quad (4.3)$$

where  $\Omega$  is expressed as

$$\begin{aligned} \Omega &= 2G^2(\sigma^2 + \Delta^2) \\ &\quad - \beta^{-1} \sum_{\pm} \sum_{n=-\infty}^{\infty} \ln [\beta^2 ((\sigma + m \pm \mu)^2 + \Delta^2 + (2n + 1)^2 \pi^2 T^2)]. \end{aligned} \quad (4.4)$$

If one takes only the lowest frequencies ( $n = 0$  and  $n = -1$ ) into account, Eq. (4.4) becomes

$$\Omega = 2G^2(\sigma^2 + \Delta^2) - 2\beta^{-1} \ln ((\sigma + m \pm \mu)^2 + \Delta^2 + \pi^2 T^2) - 2\beta^{-1} \ln \beta^2. \quad (4.5)$$

In comparison to the KTV model Eq. (2.14), it is noted that the definition of temperature is different from that of the VJ model. Let us consider the high temperature limit, where the approximation in the KTV model with only the lowest Matsubara modes incorporated is expected to be justified. For this, the summation in Eq. (4.4) is carried out to yield<sup>33)</sup>

$$\Omega = 2G^2(\sigma^2 + \Delta^2) - 2T \sum_{\pm} \log (e^{E_{\pm}/2T} + e^{-E_{\pm}/2T}) \quad (4.6)$$

$$= 2G^2(\sigma^2 + \Delta^2) - \sum_{\pm} [E_{\pm} + 2T \log (1 + e^{-\beta E_{\pm}})], \quad (4.7)$$

where  $E_{\pm} = \sqrt{(\sigma + m \pm \mu)^2 + \Delta^2}$ . By taking a limit  $T \rightarrow \infty$  of Eq. (4.6) and the effective potential of the KTV model, Eq. (2.14), we see that the VJ model is reduced to the KTV model at high temperatures, as expected, with the following identification of the two temperatures

$$4T_{\text{VJ}} = T_{\text{KTV}}^2, \quad (4.8)$$

where  $T_{\text{VJ}}$  ( $T_{\text{KTV}}$ ) denotes temperature in the VJ (KTV) model. We have checked this correspondence of temperature by looking at the values of chiral condensates  $\sigma$ . At  $T_{\text{KTV}} = 2.0$  ( $T_{\text{VJ}} = 1.0$ ), for example, a ratio of  $\sigma$  of the VJ model to that of the KTV model is 1.030 at  $\mu = 0.5$  and 1.713 at  $\mu = 1.0$ . At  $T_{\text{KTV}} = 6.0$  ( $T_{\text{VJ}} = 9.0$ ), they are 1.021 ( $\mu = 0.5$ ) and 1.086 ( $\mu = 1.0$ ). As  $T$  increases, the difference between the VJ and the KTV models become smaller, and the range where the ratio is approximately 1.0 becomes wider near  $\mu = 0$ .

By numerically solving the saddle point equations for  $m = 0.1$ , a similar phase structure to that in the right panel of Fig. 1 is obtained in the real  $\mu$  region, but with different temperature scale. The diquark condensate phase is located in the region  $0.245 \leq \mu \leq 0.519$  at  $T_{\text{VJ}} = 0$ . The location,  $\mu = 0.245$ , of the lower critical point is in fairly good agreement with a lowest perturbative calculation with a small parameter  $m$ ,  $\mu_c^2 = m/(2G^2)$  ( $\mu_c = 0.223$ ). This region closes itself at  $T_{\text{VJ}} = 0.194 (\equiv \tilde{T}_D)$ . A cross over line starts at  $(\mu, T_{\text{VJ}}) = (0.34, 0.194)$  and moves towards higher  $T$  and smaller  $\mu$  region as shown in Fig. 9, crossing

the  $T$ -axis at  $\mu = 0$  and  $T_{VJ} = 0.35 (\equiv \tilde{T}_{co})$ . It is noted that if one uses the relation Eq. (4.8), these values are in good agreement with the corresponding temperature of the KTV model;  $(T_D)^2/4 = 0.891^2/4 = 0.198$ , and  $(T_{co})^2/4 = 1.18^2/4 = 0.348$ . In the imaginary  $\mu = i\phi$

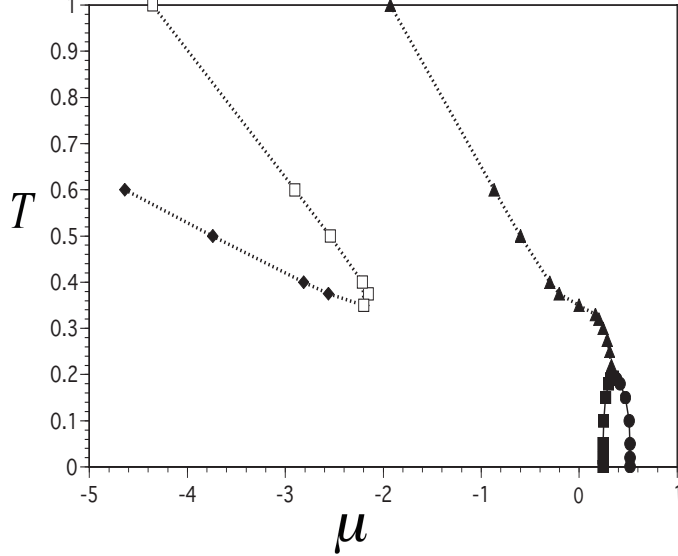


Fig. 9. Phase structure in  $\mu - T$  plane. In the imaginary  $\mu$  region, additional chiral susceptibility peaks appear due to the periodicity  $2\pi$  in  $\theta = \phi/T$ .  $m = 0.1$ . Solid and dotted lines indicate the second order critical line and cross over, respectively. Negative side of the horizontal axis indicates the imaginary chemical potential,  $i|\mu|$ .

Table VII. Values of data and the results of various fits at real values of  $\mu$  for  $T_{VJ} = 0.15$  in the VJ model. The range of used data is  $0.0 < \phi < 0.3$  and  $\Delta\phi = 0.01$ . The lower (higher) critical point of the diquark condensation exists at  $\mu = 0.270(0.472)$ .

	$\mu = 0.0$	$\mu = 0.1$	$\mu = 0.2$	$\mu = 0.3$	$\mu = 0.4$	$\mu = 0.5$
data	0.47942	0.47414	0.45345	0.29623	0.10337	0.03243
4th degree	0.47955	0.47473	0.45812	0.42327	0.35944	0.25159
6th degree	0.47944	0.47426	0.45512	0.40878	0.30490	0.08376
8th degree	0.47943	0.47417	0.45409	0.40047	0.25671	-0.13064
10th degree	0.47942	0.47415	0.45384	0.39884	0.24591	-0.21725
ratio	0.47938	0.47387	0.45062	0.34727	0.99233	0.63672

region, the VJ model respects  $2\pi$  symmetry in  $\theta \equiv \phi/T$ , in contrast to the KTV model. This is seen, when one sets  $\Delta = 0$  in the imaginary  $\mu$  region, in the the effective potential

$$\Omega = 2G^2\sigma^2 - 2 \sum_{\pm} \log \left( \exp \left[ \frac{\sigma + m}{2T} \pm i\frac{\theta}{2} \right] + \exp \left[ -\frac{\sigma + m}{2T} \mp i\frac{\theta}{2} \right] \right), \quad (4.9)$$

Table VIII. Values of data and the results of various fits at real values of  $\mu$  for  $T_{VJ} = 0.3$  in the VJ model. The range of used data is  $0.0 < \phi < 0.3$  and  $\Delta\phi = 0.01$ . A susceptibility peak is located at  $\mu = 0.245$ .

	$\mu = 0.0$	$\mu = 0.1$	$\mu = 0.2$	$\mu = 0.3$	$\mu = 0.4$	$\mu = 0.5$
data	0.28040	0.26792	0.23090	0.17619	0.12217	0.08200
4th degree	0.28029	0.26739	0.22674	0.15250	0.0349	-0.13954
6th degree	0.28038	0.26776	0.22908	0.16381	0.0775	-0.0853
8th degree	0.28040	0.26790	0.23076	0.17741	0.1564	0.34229
10th degree	0.28040	0.26792	0.23113	0.18232	0.20021	0.62457
ratio	0.28026	0.26725	0.22569	0.14681	0.01016	-0.23318

due to the summation  $\sum_{\pm}$  over positive and negative Matsubara frequencies, where  $T = T_{VJ}$ . The cross over line stated above crosses the  $T$ -axis at  $\tilde{T}_{co}$  and rises almost linearly. In addition to this, pairs of cross over lines appear, starting at  $(\phi = 2n\pi, T_{VJ} = \tilde{T}_{co})$ . In the low temperature region, the susceptibility peak appeared in the KTV model (subsection 2.2.2), although it is very broad and low, does not appear. So, this structure of the peak is due to the approximation limiting the Matsubara frequencies.

For the purpose of the analytic continuation, we studied the model by dividing the temperature into the three regions as in the previous section:  $T_{VJ} < \tilde{T}_D$  (region I),  $\tilde{T}_D \leq T_{VJ} < \tilde{T}_{co}$  (region II) and  $\tilde{T}_{co} \leq T_{VJ}$  (region III). At temperatures in region I, the analytic continuation hits the lower critical point of the diquark condensate phase at  $\mu = \mu_{c1}$ . Up to this point, both of the polynomial and ratio types of fit work but beyond it the fits break down. The results for  $T_{VJ} = 0.15$  is listed in Table VII. At this temperature,  $\mu_{c1} = 0.270$ . At  $\mu = 0.25, 0.27, 0.29$ , for example, the relative difference between the data and the 10th degree polynomial (ratio) type of fit are 0.58% (2.19%), 1.48% (3.54%), 23.15% (11.76%). In region II, we chose  $T_{VJ} = 0.3$ . At this temperature, a susceptibility peak is located at  $\mu = 0.245$ . In the similar way to the KTV case, both of the polynomial (with degree 4 to 10) and the ratio types of fit work well up to a point slightly higher than the cross over point, but beyond this point all extrapolations rapidly deviate from the data. The results for  $T_{VJ} = 0.3$  is listed in Table VIII. In contrast to these results, quite different results are obtained in region III. Figure 10 indicates the behaviors at  $T_{VJ} = 0.5$ . See also Table IX. Although the polynomial type of fits show very slow convergence, the ratio type works very well, in agreement with the results in the KTV model in the previous section. The truncation of the Matsubara sum does not affect the properties of the chiral condensate at temperatures higher than the pseudo critical temperature. This fact may suggest that it is rather general feature

in accordance with the results of MC simulations.<sup>10)</sup> The values of the fitting parameters used for all the temperatures are summarized in Table X.

@

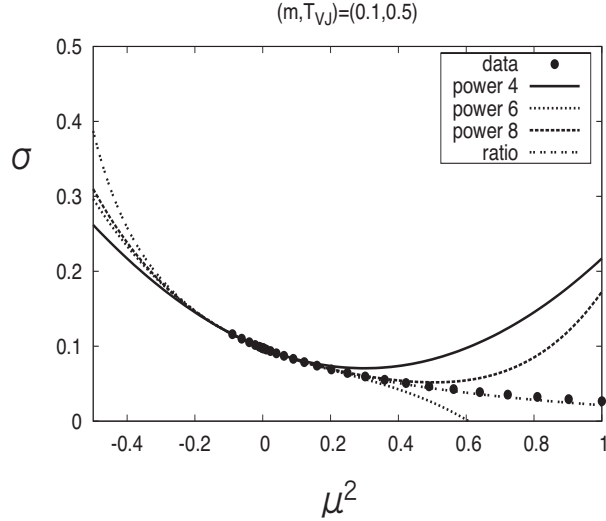


Fig. 10. Analytical continuation of chiral condensate at  $T_{VJ} = 0.5$  in the VJ model for  $m=0.1$ .

Table IX. Values of data and the results of various fits at real values of  $\mu$  for  $T_{VJ} = 0.5$  in the VJ model. The range of used data is  $0.0 < \phi < 0.3$  and  $\Delta\phi = 0.01$ .

	$\mu = 0.0$	$\mu = 0.2$	$\mu = 0.4$	$\mu = 0.6$	$\mu = 0.8$	$\mu = 1.0$
data	0.09747	0.09064	0.07403	0.05513	0.03231	0.02671
4th degree	0.09748	0.09078	0.07644	0.07166	0.10515	0.21708
6th degree	0.09747	0.09063	0.07356	0.04831	-0.00952	-0.19261
8th degree	0.09747	0.09064	0.07406	0.05638	0.05750	0.17265
10th degree	0.09747	0.09064	0.07406	0.05637	0.05740	0.17187
ratio	0.09747	0.09061	0.07374	0.05391	0.03589	0.02131

## §5. Summary

We studied analytic continuation in two-color QCD in terms of the chiral RMT with the lowest Matsubara frequencies as the temperature effect. In each of the three different temperature regions, we used polynomial and ratio types of fitting functions for the chiral condensate. In the temperature region higher than the pseudo critical point at  $\mu = 0$ , the ratio type of fit works well, while the power types show slow convergence. This is the same

Table X. Parameters of various fits of the chiral condensate in the VJ model in accordance to  $\sigma(\phi) = A + B\phi^2 + C\phi^4 + D\phi^6 + E\phi^8 + F\phi^{10}$  (polynomial; p) or  $\sigma(\phi) = \frac{A+B\phi^2}{1+C\phi^2}$  (ratio; r). Note that blank columns stand for terms not included in the fit.

$T_{\text{VJ}}$	Fit	A	B	C	D	E	F	d.o.f.	$\chi^2/\text{d.o.f.}$
0.15	p	0.47955	-0.46416	-1.79061				28	$1.23052 \times 10^{-8}$
	p	0.47944	-0.49064	-2.65467	-6.8544			27	$1.27281 \times 10^{-10}$
	p	0.47943	-0.49517	-2.92689	-11.9795	-29.7373		26	$1.54657 \times 10^{-12}$
	p	0.47942	-0.49592	-2.99819	-14.3132	-60.5581	-141.322	25	$2.02449 \times 10^{-14}$
	r	0.47938	-3.984	-7.24552				28	$2.44716 \times 10^{-9}$
0.3	p	0.28029	-1.27399	-1.62144				28	$7.7485 \times 10^{-9}$
	p	0.28038	-1.25332	-0.94699	5.35106			27	$3.38165 \times 10^{-10}$
	p	0.28040	-1.24591	-0.50153	13.7362	48.6624		26	$1.36635 \times 10^{-12}$
	p	0.28040	-1.24521	-0.43433	15.9355	77.7099	133.191	25	$1.03238 \times 10^{-14}$
	r	0.28026	-1.70342	-1.50248				28	$1.54665 \times 10^{-8}$
0.5	p	0.09748	-0.17932	0.29892				28	$3.40922 \times 10^{-11}$
	p	0.09747	-0.18072	0.25322	-0.36259			27	$1.35924 \times 10^{-14}$
	p	0.09747	-0.18067	0.25605	-0.30932	0.30912		26	$1.91676 \times 10^{-20}$
	p	0.09747	-0.18067	0.25605	-0.30933	0.30898	-0.00063	25	$1.99022 \times 10^{-20}$
	r	0.09747	-0.04686	1.37552				28	$1.554 \times 10^{-12}$

feature as that found in the study of MC simulations.<sup>10)</sup> In order to check whether this result may be affected by an approximation involved in this RMT model, we also studied a RMT model incorporating all the Matsubara frequencies<sup>33)</sup> and found that the same result is obtained in this temperature region. It might thus be rather general behavior, and reflect some non trivial dynamics of the quark gluon plasma with strong correlations.<sup>35)</sup> It is interesting that study in the imaginary  $\mu$  region may also provide useful information on the phase structure in the real  $\mu$  region.<sup>36)</sup> It would then be encouraging to study three-color QCD in terms of RMT. The results of this analysis will be reported in the forthcoming paper. We also investigated analytic continuation of the pseudo critical line. Its behavior is also similar to that in the MC simulations.<sup>11)</sup>

In view of the phase structure, some drawbacks of the RMT models should be mentioned. The first is a tricritical point of the diquark condensate transition,<sup>17),21)</sup> which is missing in the RMT models. Because of their mean field nature, the first order phase transition at higher temperature side along the critical line is not detected. This concerns our region I,

where the analytic continuation breaks down at the critical line in any case, irrespective of the order of the transition. The second is a matter of the saturation of the interactions, which manifests as a decreasing behavior of the diquark condensation for  $\mu > \mu_{c1}$ , as discussed in section 2. Temperatures in region III are outside of the region (region I) where the saturation concerns in our analysis, so we expect that the above stated behaviors in region III would be little affected, or that even if affected, it would occur in the much larger  $\mu$  region. The last is the Roberge-Weiss symmetry, which reflects the center symmetry of the gauge group. This symmetry periodically induces critical lines at  $\theta(= \phi/T) = (k + 1/2)\pi$  ( $k$ : integer). In the RMT model, this symmetry is missing. The existence of the critical line closest to the  $\mu = 0$  axis affects the analytic continuation.<sup>10)</sup> In terms of the imaginary  $\mu$  variable,  $\phi = T\pi/2$ , the distance from the  $\mu = 0$  axis is proportional to  $T$ , and its effect becomes less serious at higher temperatures. This may be a reason why the RMT model leads to the same conclusions as the MC simulations at higher temperature regions. In the lower temperature region, on the other hand, missing RW symmetry may cause a discrepancy between the lattice gauge theory and the corresponding RMT model. In fact, a use of a periodic fitting function is suggested in the low temperature region in the study of MC simulations.<sup>10)</sup> This is, however, beyond the scope of the present analysis, unless some RMT model with the RW symmetry is considered.

### Acknowledgments

We are grateful to M. Imachi, H. Kouno, M. Tachibana and A. Wipf for useful discussion.

### References

- 1) C.R. Allton, S. Ejiri, S.J. Hands, O. Kaczmarek, F. Karsch, E. Laermann, Ch. Schmidt and L. Scorzato, Phys. Rev. **D66** (2002), 074507.  
C.R. Allton, M.Döring, S. Ejiri, S.J. Hands, O. Kaczmarek, F. Karsch, E. Laermann, K. Redlich, Phys. Rev. **D71** (2005), 054508.
- 2) R.V. Gavai and S. Gupta, Phys. Rev. **D68** (2003), 034506.
- 3) Z. Fodor and S.D. Katz, Phys. Lett. **B534** (2002), 87; JHEP**03** (2002), 014.
- 4) Ph. de Forcrand and O. Philipsen, Nucl. Phys. **B642** (2002), 290; Nucl. Phys. **B673** (2003), 170.
- 5) M. D’Elia and M.P. Lombardo, Phys. Rev. **D67** (2003), 014505; Phys. Rev. **D70** (2004), 074509.
- 6) P. Giudice and A. Papa, Phys. Rev. **D69** (2004), 094509.
- 7) V. Azcoiti, G. Di Carlo, A. Galante and V. Laliena, Nucl. Phys. **B723** (2005), 77;

- JHEP **12** (2004), 010.
- 8) H. S. Chen and X. Q. Luo, Phys. Rev. **D72** (2005), 034504.
  - 9) L. K. Wu, X. Q. Luo and H. S. Chen, Phys. Rev. **D76** (2007), 034505.
  - 10) P. Cea, L. Cosmai, M. D’Elia and A. Papa, JHEP **02** (2007), 066.
  - 11) P. Cea, L. Cosmai, M. D’Elia and A. Papa, Phys. Rev. **D77** (2008), 051501(R); arXiv:0812.2777 [hep-lat].
  - 12) A. Nakamura, Phys. Lett. **B149** (1984), 391.
  - 13) E. Dagotto, F. Karsch and A. Moreo, Phys. Lett. **B169** (1986), 421.
  - 14) E. Dagotto, A. Moreo and U. Wolff, Phys. Lett. **B186** (1987), 395.
  - 15) J.B. Kogut, M.A. Stephanov, and D. Toublan, Phys. Lett. **B464** (1999), 183.
  - 16) J.B. Kogut, M.A. Stephanov, D. Toublan, J.J.M. Verbaarschot and A. Zhinitsky, Nucl. Phys. **B582** (2000), 477.
  - 17) J.B. Kogut, D. Toublan and D.K. Sinclair, Phys. Lett. **B514** (2001), 77; Nucl. Phys. **B642** (2002), 181.
  - 18) K. Splittorff, D.T. Son and M.A. Stephanov, Phys. Rev. **D64** (2001), 016003.
  - 19) J.B. Kogut, D.K. Sinclair, S.J. Hands and S.E. Morrison, Phys. Rev. **D64** (2001), 094505.
  - 20) J.B. Kogut, D. Toublan and D.K. Sinclair, Phys. Rev. **D68** (2003), 054507.
  - 21) K. Splittorff, D. Toublan and J.J.M. Verbaarschot, Nucl. Phys. **B639[FS]** (2002), 524.
  - 22) J. Wirstam, J.T. Lenaghan and K. Splittorff, Phys. Rev. **D67** (2003), 034021.
  - 23) S. Muroya, A. Nakamura and C. Nonaka, Phys. Lett. **B551** (2003), 305
  - 24) C. Ratti and W. Weise, Phys. Rev. **D70** (2004), 054013.
  - 25) Y. Nishida, K. Fukushima and T. Hatsuda, Phys. Rept. **398** (2004), 281.
  - 26) B. Allés, M. D’Elia and M.P. Lombardo, Nucl. Phys. **B752** (2006), 124.
  - 27) K. Fukushima and K. Iida, Phys. Rev. **D76** (2007), 054004.
  - 28) For a review, see J.J.M. Verbaarschot and T. Wettig, Ann. Rev. Nucl. Part. Sci. **50** (2000), 343.  
G. Akemann, Int. J. Mod. Phys. **A22** (2007), 1077.
  - 29) M. A. Halasz, A. D. Jackson, R. E. Shrock, M. A. Stephanov and J.J.M. Verbaarschot, Phys. Rev. **D58** (1998), 096007.
  - 30) Y. Shinno and H. Yoneyama , in preparation.
  - 31) B. Klein, D. Toublan and J.J.M. Verbaarschot, Phys. Rev. **D68** (2003), 014009.
  - 32) B. Klein, D. Toublan and J.J.M. Verbaarschot, Phys. Rev. **D72** (2005), 015007.
  - 33) B. Vanderheyden and A.D. Jackson, Phys. Rev. **D64** (2001), 074016.
  - 34) A. Roberge and N. Weiss, Nucl. Phys. **B275[FS17]** (1986), 734.



- 35) M. D'Elia, F. Di Renzo and M.P. Lombardo, Phys. Rev. **D76** (2007), 114509.
- 36) Y. Sakai, K. Kashiwa, H. Kouno and M. Yahiro, Phys. Rev. **D77** (2008), 051901.  
Y. Sakai, K. Kashiwa, H. Kouno, M. Matsuzaki and M. Yahiro, arXiv:0902.0487 [hep-ph].